



Published in final edited form as:

IEEE Trans Med Imaging. 2018 July ; 37(7): 1653–1663. doi:10.1109/TMI.2017.2787589.

TRACE: A Topological Graph Representation for Automatic Sulcal Curve Extraction

Ilwoo Lyu*,

Electrical Engineering and Computer Science, Vanderbilt University, Nashville, TN 37235 USA

Sun Hyung Kim,

Department of Psychiatry, The University of North Carolina, Chapel Hill, NC 27599, USA.

Neil D. Woodward,

Department of Psychiatry, Vanderbilt University, Nashville, TN 37235 USA.

Martin A. Styner,

Department of Psychiatry, The University of North Carolina, Chapel Hill, NC 27599, USA.

Bennett A. Landman

Electrical Engineering and Computer Science, Vanderbilt University, Nashville, TN 37235 USA

Abstract

A proper geometric representation of the cortical regions is a fundamental task for cortical shape analysis and landmark extraction. However, a significant challenge has arisen due to the highly variable, convoluted cortical folding patterns. In this paper, we propose a novel topological graph representation for automatic sulcal curve extraction (TRACE). In practice, the reconstructed surface suffers from noise influences introduced during image acquisition/surface reconstruction. In the presence of noise on the surface, TRACE determines stable sulcal fundic regions by employing the line simplification method that prevents the sulcal folding pattern from being significantly smoothed out. The sulcal curves are then traced over the connected graph in the determined regions by the Dijkstra's shortest path algorithm. For validation, we used state-of-the-art surface reconstruction pipelines on a reproducibility dataset. The experimental results showed higher reproducibility and robustness to noise in TRACE than the existing method (Li *et al.* 2010) with over 20% relative improvement in error for both surface reconstruction pipelines. In addition, the extracted sulcal curves by TRACE were well-aligned with manually delineated primary sulcal curves. We also provided a choice of parameters to control quality of the extracted sulcal curves and showed the influences of the parameter selection on the resulting curves.

Keywords

cortical surface; line simplification; shortest path; sulcal curve; topological graph; valley detection

* ilwoo.lyu@vanderbilt.edu.

I. Introduction

With the recent advent of 3D cortical surface reconstruction [1]–[4], fundamental geometric landmarks such as local curvature are readily accessible and thus commonly used in 3D cortical surface-based analyses. Of many potential geometric properties, sulcal landmarks are one of the most invariant, stable features across cortical regions [5]. There have been an increasing number of studies that focus on brain developmental studies and pathological disorders via a sulcal region analysis over the human cortex [6]–[14]. Also, the landmarks of the primary sulcal regions have been widely used as robust features for cortical surface registration [15]–[22]. However, a main challenge comes from the nature of the cortical folding patterns with its highly complex and variable shapes, which hampers the consistency of cortical folding analyses. As a prerequisite, thus, a key aspect to such analyses is to determine and represent the cortical folding regions of interest in a consistent manner.

Regional parcellation is most prevalent for the sulcal region recognition for which a shape correspondence is employed to transfer cortical labels of a template (or reference) model into target surfaces [23]–[25]. However, this approach significantly depends on the quality of surface correspondence and often suffers from inaccurate regional boundaries due to high sulcal variability across subjects. Despite the lack of formal definition of the sulcal regions (more precisely, an unclear boundary between sulci and gyri), sulcal curves can be defined along the sulcal fundic regions anatomically. In this context, the sulcal fundic regions are represented as a set of curves without employing any predefined template model. Although a main advantage comes from no template selection bias, the approach casts a critical question of how to define/extract the sulcal fundic regions in a consistent way. In earlier work [26], a model-based fitting method such as deformable curve was proposed for several primary sulci; however, this approach has difficulty incorporating individual curve variability (e.g., the number of curve segments in the inferior temporal sulcus). Thus, the geometry-based sulcal curve extraction could be more desirable.

Curvature measures have an advantageous property in terms of capturing local geometry with the formal definition at a given point on the surface. One might determine appropriate sulcal regions by applying simple thresholding of the local curvature. However, relying only on the curvature threshold potentially overestimates (or underestimates) the sulcal fundic regions since curvature thresholding is quite sensitive to threshold selection as well as the presence of noise over the sulcal regions in general. To alleviate that, a smoothing kernel can be employed, which needs to be chosen carefully as otherwise large portions of the surface are smoothed out. Even if an optimal curvature threshold/smoothing kernel size is determined, a spatial coherence still needs to be considered for sulcal curve extraction. Several attempts at curvature-based sulcal region extraction have been reported in [27]–[29]. Unfortunately, sulcal curves do not always pass through points associated with a maximal curvature as pointed out in [30].

Graphical model-based sulcal curve extraction methods have been proposed in [30], [31]. In [31], the cortical surface is regarded as a connected graph with curvature-based weights, and the shortest path is computed between two endpoints. [30] extended the idea of [31] by utilizing a geodesic density map to address the endpoint selection problem. In this method,

the sulcal curves are obtained by a frequency of each vertex across all possible paths given regions. Overall, these approaches assume that the shortest paths are highly likely to have an intersection with sulcal fundic regions. However, the resulting curves are (partially) the Dijkstra's shortest path of a 1-ring-neighborhood graph, which is not exactly the same as the corresponding geodesic path on the surface. Moreover, this might be sensitive to the quality of surface tessellation. For example, the shortest path must pass one of the neighboring vertices that could not be located in optimal fundic regions.

There have been skeleton-based methods [32]–[35]. [33] extracted sulcal curves as a skeleton via solving an Eikonal equation (a special form of the Hamilton-Jacobi equation) on the cortical surface. They defined sulcal points from flux of the geodesic distance field (solution of the Eikonal equation) and pruned skeletons as a result. Quality of the extraction could be sensitive to local noise in computing the flux. [34] proposed curvature-based sulcal curves. Similar to [33] they used a sulcal depth map to define source of the wavefront propagation and then solved the Hamilton-Jacobi equation for anisotropic geodesics. However, this method requires careful parameter tuning to determine candidate points that belong to potential sulcal curves. In particular, since the initial seed regions for the wavefrontal propagation are based on a sulcal depth map, the sulcal curve extraction could be quite sensitive to the initial definition of the seed regions especially in wide sulcal fundi such as the Sylvian fissure. As an alternative skeletonization of the cortical folding, sulcal depth information has also been utilized for sulcal curve extraction [32]. They used sulcal depth to select candidate sulcal points and connected/refined them to have a set of curve segments by defining endpoints.

We propose a novel topological graph representation for automatic sulcal curve extraction (TRACE). We mainly focus on 1) stable sulcal fundic point detection and 2) consistent sulcal curve extraction by connecting the detected sulcal points. For the sulcal point detection, we use the line simplification method [36], [37], which consistently selects a minimum sufficient number of stable (extremal) points from a given shape in the presence of noise to represent the original shape. Stable sulcal points are thus detected in a robust way to noise. For the sulcal curve extraction, a partially connected graph is constructed in the detected regions, and edge weights are assigned based on geodesic distances. The optimal sulcal curves are finally traced over the graph by the Dijkstra's algorithm [38]. In contrast to [30], [31], TRACE is not limited to a 1-ring neighborhood, resulting in more flexible curves. This paper extends [39] with the following key contributions: 1) novel sulcal curve extraction method, 2) detailed technical descriptions of the algorithm and parameter choice, and 3) extensive validation on two surface reconstruction pipelines for reproducibility and robustness to noise as well as a comparison with manual delineation compared to the existing method [35].

II. Background

A. Line Simplification

The line simplification method proposed by [36], [37]. The method recursively approximates a polyline/polygon with a small number of the original points. Here is a brief summary of the line simplification method [36], [37]. At each recursion step, two endpoints \mathbf{p}_0 and \mathbf{p}_1 of

a given polyline are connected as a horizontal (base) line. Then, the extremal point $\hat{\mathbf{p}}$ along the polyline with the maximum distance from the line is selected as follows:

$$\hat{\mathbf{p}} = \arg \max_{\mathbf{p}} \|(\mathbf{p}_1 - \mathbf{p}_0) \times \mathbf{p}\| \cdot \|\mathbf{p}_1 - \mathbf{p}_0\|^{-1}. \quad (1)$$

The initial curve is split into two segments at the selected point $\hat{\mathbf{p}}$ and the two endpoints. The method is then recursively applied to the two curve segments until the maximum distance is below a given tolerance δ . Note that there can be various point selection strategies rather than the maximum distance [40], depending on the application. The algorithm has been widely applied in the field of data compression, digital cartography, and denoising over range data from robotic sensors. One of the main advantages is the denoising effect without a significant loss of valley- or ridge-like points compared to a standard smoothing noise (e.g., low-pass filter). This property could be also preferable in detecting cortical sulcal curves within sulcal fundic (valley) regions in the presence of noise. The algorithm has $\mathcal{O}(N^2)$ complexity without optimization, which can be efficiently solved proportional to $\mathcal{O}(N \log N)$ [41], where N is the number of the points. Fig. 1 shows an example of the line simplification method.

B. Geodesic Distance

A geodesic distance can be computed via formulating the wavefront propagation over the surface model. Given a medium Ω and its boundary $\partial\Omega$ (tangent space of the cortical surface with a speed at every point for example) in \mathbb{R}^2 , the minimum travel-time from one (or multiple) source $\mathbf{x}_0 \in \partial\Omega$ to a point $\mathbf{x} \in \Omega$ in the medium, $t(\mathbf{x})$, follows the propagation equation for some propagation speed functional F :

$$\begin{aligned} \|\nabla t(\mathbf{x})\| F\left(\mathbf{x}, \frac{\nabla t(\mathbf{x})}{\|\nabla t(\mathbf{x})\|}\right) &= 1, & \mathbf{x} \in \Omega \subset \mathbb{R}^2, \\ t(\mathbf{x}) &= 0, & \mathbf{x} \in \partial\Omega. \end{aligned} \quad (2)$$

This formulation is the so-called Hamilton-Jacobi partial differential equation (H-J PDE). By letting $F = c \in \mathbb{R}^+$ for $\forall \mathbf{x} \in \Omega$, this simplifies the H-J PDE to

$$\|\nabla t(\mathbf{x})\| c(\mathbf{x}) = 1. \quad (3)$$

Such a special case of the H-J PDE is known as the Eikonal equation that solves the wavefront propagation with a constant speed functional c in every direction. For $c = 1$ the solution is thus equivalent to the geodesic distance from $\partial\Omega$. Efficient solvers called fast marching [42]–[44] are well developed for solving the Eikonal equation. In this work, we employed the ordered upwind method with $\mathcal{O}(N \log N)$ complexity akin to the Dijkstra's shortest path algorithm [38], where N is the number of discrete points over Ω , proposed by [44].

III. Methods

A. Objective

Given a triangulated mesh Ω of the cortical surface with a set of vertices V , the objective is to find a subset $U \subseteq V$ that consists of sulcal points located at the deepest sulcal regions so as to represent sulcal curves. The entire process consists of two main components: 1) sulcal point detection to represent stable sulcal fundic regions and 2) sulcal curve extraction on the connected graph of the detected sulcal points. Briefly, stable sulcal points are selected along the sulcal fundic regions by the line simplification method, and then the Dijkstra's algorithm yields sulcal curves as optimal paths over the graph. A schematic overview of TRACE is illustrated in Fig. 2. Table I summarizes a glossary of parameters used in this paper.

B. Sulcal Point Detection

Relying only on the curvature measurements typically overestimates (or underestimates depending on a threshold) the sulcal regions from which sulcal curves are extracted as shown in Fig. 3. Also, the curvature measurements are quite sensitive to local noise. Thus, the selected candidate points by curvature thresholding need to be refined for better estimation of the sulcal fundic regions in terms of 1) the reduced number of the candidate points for compact sulcal fundic representation and 2) robustness to local noise. To further refine these regions, therefore, we use the line simplification method.

A set of candidate points is first selected via relatively generous thresholding of the maximum principal curvature at each location $\in \Omega$ by filtering convex (gyral) regions. Then, to refine sulcal fundic regions, we used the line simplification method. Since the method was originally designed for 1D polylines, a cutting plane is determined orthogonal to the second principal direction at each point $\mathbf{v} \in V$ to maximize its curvature. A point is added to U if it is preserved after the line simplification process.

1) Slicing and Contour Extraction—To extend the idea of the line simplification method to 2-manifolds, a novel definition is necessary for most meaningful lines from the surface at every location. Here, TRACE utilizes a planar intersection along a given direction. To utilize differential geometry, we follow the convention in [45]. In particular, at a given point $\mathbf{v} \in V \subset \Omega$, the normal curvature with respect to a given tangent direction \mathbf{T} at \mathbf{v} is obtained by

$$k(\mathbf{T}) = D_{\mathbf{T}}\mathbf{N} \cdot \mathbf{T}, \quad (4)$$

where $D_{\mathbf{T}}$ denotes a directional derivative with respect to \mathbf{T} , and \mathbf{N} is the surface normal at \mathbf{v} . Since the objective is to check if \mathbf{v} is potentially identified as a sulcal point, a proper tangent direction \mathbf{T} needs to be determined to find a maximum curvature k in the tangent space, in which the surface bends highly along its sulcal fundus. The minimum curvature is defined along the direction associated with the second principal curvature k_2 k_1 , where k_1 is the first principal curvature. We use [46] for the curvature approximation. Thus, the second principal direction defines a plane normal at each vertex $\mathbf{v} \in V$. Let \mathbf{T}_{k_2} be the second principal direction associated with k_2 at \mathbf{v} . Thus, the plane equation is given by

$$\mathbf{T}_{k_2} \cdot (\mathbf{x} - \mathbf{v}) = 0. \quad (5)$$

We assume that there are neither holes nor self-intersections on the surface. Thus, a cut between the plane and the surface yields a (or multiple) closed loop with no self-intersection. Here we propose a discrete version of [47] to produce a contour at any location of the surface. On the discrete surface model, a planar intersection test requires an exhaustive, computationally demanding test for every edge of the surface to meet a condition in (5). Thanks to an edge culling technique, this can be efficiently addressed by an incorporation of hierarchical axis-aligned bounding boxes (AABB). Finally, by sorting these intersections in counter-clockwise order with respect to the curve tangent $(\mathbf{x} - \mathbf{v})$, the ordered closed loop(s) is easily obtained for $\forall \mathbf{v} \in \Omega$. Fig. 4 illustrates an example of contour extraction for both a synthetic and an actual cortical surface. The principal direction captures the maximum curvature as an optimal representation of the sulcal fundus in terms of its local surface bending.

2) Candidate Point Filtering—Given a contour at $\mathbf{v} \in \Omega$, the line simplification approach is applied to the contour to select the minimum sufficient number of extremal points that represent the contour itself and to check if \mathbf{v} is filtered out after the line simplification method. In this problem setting, two endpoints are determined by finding the largest distance on the plane of \mathbf{T}_{k_2} among all possible pairs of points of the contour to split it into two longest possible curves by finding two extremal points as stated in [36], [37]. The line simplification method is then applied to one of the two curves that contains the testing point \mathbf{v} . If \mathbf{v} is reported as an extremal point by the line simplification method, \mathbf{v} is collected into U as a sulcal point. In Fig. 4, the endpoints are consistently selected by the line simplification method even with in the presence of noise on the surface in a robust way. Overall, TRACE collects a set of candidate points whose number varies according to a user-defined threshold value δ . Fig. 4 shows an example of sulcal points chosen by the line simplification method on smooth and noise surfaces.

C. Sulcal Curve Extraction

Although the candidate points are significantly filtered out by the line simplification method, there still exist multi-sulcal points along the sulcal fundic regions in general. To extract sulcal curves from the cortical surface, a subset of the selected sulcal points thus need to be selected for the curve extraction. In our previous work [39], the local optimal trajectory could not guarantee a unique solution, and the resulting sulcal curves depend on the endpoint selection order for the extraction. In this section, we propose consistent sulcal curve extraction regardless of the endpoint selection order. In brief, we construct a graph of the detected sulcal points to find optimal paths as sulcal curves. However, finding optimal paths from a complete graph of the sulcal points is computationally demanding. We instead create a partially connected graph G that disconnects two points having a geodesic distance between them longer than a given threshold r . From G , we select endpoints and geodesic distances between them are computed via the Dijkstra's shortest path algorithm. Fig. 5 illustrates the proposed graph construction and geodesic paths.

1) Geodesic Radial Functional—For $\forall \mathbf{u} \in U$, sulcal points are collected within a geodesic distance r defined by an indicator functional:

$$R(\mathbf{u}, \mathbf{v}; r) = \begin{cases} 1 & \text{if } d_{\mathbf{u}}(\mathbf{v}) \leq r, \\ 0 & \text{otherwise,} \end{cases} \quad (6)$$

where $d_{\mathbf{u}}(\mathbf{v})$ is a geodesic distance from \mathbf{u} to $\mathbf{v} \in \Omega$. By setting \mathbf{u} to a source of the wavefront propagation, the geodesic distance $d_{\mathbf{u}}$ can be computed by the Eikonal equation (see (2)).

$$\|\nabla d_{\mathbf{u}}(\mathbf{x})\| = 1. \quad (7)$$

The solution provides a geodesic distance $d_{\mathbf{u}}$ from \mathbf{u} to all locations of Ω . The sulcal points have geodesic paths to each other within a radius of r in (6). For convenience, we let $R_{\mathbf{u}}(\mathbf{u}) = \{\mathbf{s} | \mathbf{s} \in U \text{ and } R(\mathbf{u}, \mathbf{s}; r) = 1\}$ to represent a set of neighboring sulcal points that belong to \mathbf{u} .

2) Graph Construction—The construction of a complete graph of U is practically intractable. For $\forall \mathbf{u}$, we instead create a complete subgraph that connects every possible pair within a radius of r to create a partially connected graph G of U . Consequently, any Dijkstra's path has a much higher degree of freedom on G than a 1-ring neighborhood graph. To construct G , r needs to be chosen such that it sufficiently covers sulcal fundic regions. Once G is constructed, assigning a geodesic distance to each edge might be insufficient because the distance only encodes a shortest geodesic path, which lacks the curvature (smoothness) of the resulting sulcal curves as shown in Fig. 6. To take account of the curvature for curve smoothness, the edge weight is thus given by the following form of a non-negative monotonic functional:

$$w(\mathbf{u}, \mathbf{s}) = d_{\mathbf{u}}(\mathbf{s}) \cdot \exp(\ln \gamma \cdot \|(\mathbf{s} - \mathbf{u}) \times \mathbf{T}(\mathbf{u})\| \cdot \|\mathbf{s} - \mathbf{u}\|^{-1}), \quad (8)$$

where $\ln \gamma$ is a regularization of the curvature by which a scalar of the edge weight varies from 1 to γ , and $\mathbf{T}(\mathbf{u})$ is the tangent vector of the sulcal curve at \mathbf{u} . This implies that a neighboring point of \mathbf{u} is penalized if the point is away from the tangent direction $\mathbf{T}(\mathbf{u})$; the higher γ , the more local-curvature sensitivity. Note that the sulcal curve is obtained as a geodesic path if $\gamma = 1$. Unfortunately, $\mathbf{T}(\mathbf{u})$ is unknown since it should be obtained from the sulcal curve to be estimated. We instead estimate $\hat{\mathbf{T}}(\mathbf{u})$ from the local principal directions at \mathbf{u} and \mathbf{s} . To determine a unique tangent direction between \mathbf{u} and \mathbf{s} , we compute the mean of the two local principal directions on the unit sphere by the Rodrigues rotation formula:

$$\begin{aligned} \hat{\mathbf{T}}(\mathbf{u}) = & \mathbf{T}_{k_2}(\mathbf{u}) \cos \theta_{\times} + \left(\mathbf{T}_{k_2}(\mathbf{u}) \times \mathbf{T}_{\times} \right) \sin \theta_{\times} \\ & + \mathbf{T}_{\times} \cdot \left(\mathbf{T}_{\times} \cdot \mathbf{T}_{k_2}(\mathbf{u}) \right) (1 - \cos \theta_{\times}), \end{aligned} \quad (9)$$

where

$$\mathbf{T}_\times = \frac{\mathbf{T}_{k_2}(\mathbf{u}) \times \mathbf{T}_{k_2}(\mathbf{s})}{\|\mathbf{T}_{k_2}(\mathbf{u}) \times \mathbf{T}_{k_2}(\mathbf{s})\|}, \quad (10)$$

and

$$\theta_\times = \frac{1}{2} \arccos(\mathbf{T}_{k_2}(\mathbf{u}) \cdot \mathbf{T}_{k_2}(\mathbf{s})). \quad (11)$$

We assume $2\theta_\times = \pi/2$ without loss of generality. In this way, the average tangent vector $\widehat{\mathbf{T}}(\mathbf{u})$ guarantees that the edge weight between \mathbf{u} and \mathbf{s} is symmetric, which enforces G to be undirected.

3) Endpoint Detection—In order to connect the candidate points into complete curves from G , potential endpoints of (yet unknown) sulcal curves need to be estimated, which are later set to starting points of the Dijkstra's shortest path algorithm. A sulcal point \mathbf{u} is determined as an endpoint if every neighboring sulcal point $\in R_r(\mathbf{u})$ belongs to a spherical cone centered at \mathbf{u} as shown in Fig. 7. To measure the angle of the cone, we then check the maximum angle ϕ across every possible pair of $R_r(\mathbf{u})$:

$$\phi = \max_{s_1, s_2 \in R_r(\mathbf{u})} \arccos\left(\frac{\mathbf{s}_1 - \mathbf{u}}{\|\mathbf{s}_1 - \mathbf{u}\|} \cdot \frac{\mathbf{s}_2 - \mathbf{u}}{\|\mathbf{s}_2 - \mathbf{u}\|}\right). \quad (12)$$

We still need to specify the angle of the spherical cone appropriately to determine endpoints. Two general sulcal point patterns are observed: 1) The selected sulcal points typically have a quite wide distribution like locally straight line along the sulcal fundic regions (i.e., $\phi \approx 180$ degrees). 2) In contrast, the sulcal points have a biased distribution at the end of the sulcal fundic regions). The larger ϕ , the more number of endpoints, which could result in several minor branch curves though they are pruned later. From this observation, we empirically determine \mathbf{u} as an endpoint if ϕ is less than 90 degrees in a conservative manner. We let $E \subseteq U$ be the set of the endpoints determined by this way.

4) Shortest Path and Curve Pruning—The key idea is to find an optimal trajectory between endpoints. For $\forall \mathbf{u} \in E$, the curve estimation is performed on G by the Dijkstra's shortest path algorithm. In the sulcal regions having branch, there exist several shortest paths due to the existence of multi-endpoints. We choose one with the longest distance not to end up with having a path at local small branch. Since G is undirected, the shortest path is consistent regardless of the starting point order, which is guaranteed by the Dijkstra's algorithm.

The TRACE algorithm generates primary curves with several branch. We are interested in primary sulcal curves since minor branch curves are likely to vary by noise influences. For consistent curve extraction, therefore, the minor branch curves need to be pruned. For this purpose, we adapt the idea of [33]. The idea is to consider the curve length and continuity for each sulcal curve. Specifically, we measure the curve length l (geodesic on the surface) for all sulcal curves. For a branch curve, we compute the minimum angle ϕ at the junction

point across other branch curves. The sulcal curve length is then adjusted by $l \cdot \exp(\cos \varphi)$. The pruning algorithm is applied in a greedy manner until no adjusted sulcal curve length is found less than a threshold ψ . Fig. 5 shows the estimated sulcal curves from G of the sulcal points. Algorithm 1 summarizes the overall procedure of the TRACE algorithm.

D. Complexity Analysis

1) Sulcal Point Detection—The candidate points are selected by curvature threshold, which requires $\mathcal{O}(|V|)$. For each candidate point, a contoured slice is obtained via AABB tree search. The reconstruction of the AABB tree takes $\mathcal{O}(|V| \log |V|)$, and the tree search takes $\mathcal{O}(\log |V|)$. Then, the sulcal point is determined by the line simplification method in $\mathcal{O}(c \log c)$, where c is the number of points on a given contour. The total complexity is $\mathcal{O}(|V| \cdot m \log m)$ by letting $m = \max\{c\}_1^{|V|}$. In summary, the upper bound of the computational cost for the sulcal point detection is $\mathcal{O}(|V| \cdot (\log |V| + m \log m))$. Since $m \ll |V|$, the total time complexity is $\mathcal{O}(|V| \log |V|)$ by assuming $m \log m$ is constant.

2) Sulcal Curve Extraction—The graph is constructed from the detected sulcal points. Since we consider a partially connected graph, the graph construction takes $\mathcal{O}(e)$ by letting $e = |U| \cdot \max\{|R_r\}_1^{|U|}$, and each edge weight is assigned by the geodesic distance computation, i.e., $\mathcal{O}(e \log e)$. Once G is constructed, the endpoints are determined in $\mathcal{O}(|U|)$. Finally, the Dijkstra algorithm takes $\mathcal{O}(e + |U| \log |U|)$ for each endpoint. Note $\max\{|R_r\}_1^{|U|} \ll |U|$.

3) Overall Complexity—Practically, since $|U| \ll |V|$, the sulcal point detection is dominant. This yields $\mathcal{O}(|V| \log |V|)$ for total complexity of the TRACE algorithm. In terms of computation time, sulcal point detection takes about 10 mins for a 160k mesh on a single core (Intel Xeon E5–2630 2.20GHz), and the curve delineation takes 2 mins.

Algorithm 1

TRACE algorithm

Input: a set of vertices $V \subseteq \Omega$

Output: a set of sulcal curves on Ω

- 1: $U \leftarrow \emptyset$ ▷ a set of sulcal points
- 2: **for** $\mathbf{v} \in V$ **do** ▷ loop for sulcal point detection
- 3: $k_1 \leftarrow$ the first principal curvature at \mathbf{v} (4).
- 4: $\mathbf{T}_{k_2} \leftarrow$ the second principal direction at \mathbf{v} (4).
- 5: **if** $k_1 > 0.05$ **then**
- 6: Compute a contoured slice given by \mathbf{T}_{k_2} (5).
- 7: Apply the line simplification to the slice using (1).
- 8: **if** \mathbf{v} is selected by the line simplification **then**
- 9: $U \leftarrow U \cup \{\mathbf{v}\}$

```

10:   end if
11: end if
12: end for
13: Construct a partial graph  $G$  of  $U$  (6).
14: Assign edge weights to  $G$  (8) and (9).
15:  $E \leftarrow \emptyset$  ▷ a set of endpoints
16: for  $u \in U$  do ▷ loop for endpoint detection
17:   Compute the separation angle  $\phi$  in  $R_u(\mathbf{u})$  (12).
18:   if  $\phi < 90$  then
19:      $E \leftarrow E \cup \{\mathbf{u}\}$ 
20:   end if
21: end for
22: while  $E \neq \emptyset$  do ▷ loop for the Dijkstra's algorithm [38]
23:   Find the farthest endpoint from  $\mathbf{e} \in E$ .
24:   Store the trajectory between the two endpoints.
25:    $E \leftarrow E \setminus \{\mathbf{e}\}$ 
26: end while
27: Apply the pruning algorithm [33] to the sulcal curves.

```

IV. Validation

A. Materials

1) Kirby Reproducibility Dataset—In the experiment, we chose the Kirby reproducibility dataset [48] to evaluate the TRACE algorithm. Briefly, the Kirby reproducibility dataset was acquired on 21 healthy volunteers with no history of neurological disease. Scan-rescan imaging sessions with T_1 -weighted scans were acquired at the F.M. Kirby Research Center (Baltimore, MD, USA), using the MP-RAGE sequence on 3T Philips Achieva scanners at $1.0\text{mm} \times 1.0\text{mm} \times 1.2\text{mm}$ resolution (204 slices with $\text{TR}=6.7\text{ms}$, $\text{TE}=3.1\text{ms}$, flip angle= 8° , matrix= 240×256) scans. We used two surface reconstruction pipelines for validation: FreeSurfer [1] and MaCRUISE [4] on the Kirby reproducibility dataset. We created the middle surfaces of both left and right hemispheres.

2) MRIs Surfaces Curves (MSC) Dataset—We used the MSC dataset for comparison with manually labeled primary curves [49], [50]¹. The structural scans of subjects were obtained as part of a functional imaging study and comprised 12 subjects (6 males, 6 females). The subjects were scanned at the Dornsife Cognitive Neuroscience Imaging Center at the University of Southern California using a 3T Siemens MAGNETOM Trio scanner. High-resolution T_1 -weighted anatomical volumes were acquired for each subject with an MP-RAGE scan using the following protocol: $\text{TR} = 2350\text{ms}$, $\text{TE} = 4.13\text{ms}$, 192 slices, $\text{eld of view} = 256\text{mm}$, voxel size = $1.0\text{mm} \times 1.0\text{mm} \times 1.0\text{mm}$. The BrainVoyager automatic registration procedure was performed in the preprocessing. The middle cortical surfaces

¹<http://sipi.usc.edu/~ajoshi/MSC>

were then extracted by the FreeSurfer software using default parameters, and 26 primary sulcal curves were traced using the BrainSuite software.

B. Parameter Choice

1) Candidate Point Filtering—Since potential sulcal points lie along the sulcal fundic regions, they have positive maximum principal curvatures. For expediting the process, the number of extremal point tests can be reduced by choosing thresholding of curvatures. This threshold was empirically set to 0.05. Such thresholding is used just for computational efficiency. The line simplification method requires a tolerance δ . This quantity controls a level of detailed representation of each contour. Thus, δ encodes the smallest deviation between the simplified and original contours. Although δ is not exactly the same as sulcal depth, it could be highly correlated with sulcal depth while evaluating the actual sulcal point. Typically, a change of δ shows a similar behavior of sulcal depth thresholding. If δ is too large, the line simplification method leaves sulcal points located only on the deep sulcal regions, which yields a few number of sulcal curves. On the other hand, small δ sufficiently captures sulcal points along the sulcal fundic regions, while it creates a large number of sulcal points, i.e., additional minor branch curves as shown in Fig. 8. In our experiment, δ was empirically set to 2.5 *mm* on the adult cortical surfaces similar to that used in the literature [32].

2) Graph Construction—The proposed graph of sulcal points is constructed by a geodesic radial functional R , which consists of two main components: 1) partial graph construction and 2) endpoint detection. For each sulcal region, the graph needs to be connected appropriately to cover a trajectory along the sulcal fundic region. From previous findings on the adult human cortex [32], [51], the sulcal depth of the primary sulcal regions is larger than 10.0 *mm*. Also, the study [52] implies that most gyri have the width of at least 10.0 *mm*. From these observations, we chose $r = 4.0$ *mm* to sufficiently cover the sulcal fundic regions but not to simultaneously cover two sulcal regions. Note that δ is an Euclidean metric on the contoured slice, which is smaller than r though. This geodesic distance can be adjusted depending on the target population. We used the same size of r as the graph construction for the endpoint detection. A small value of r typically detects multi-endpoints in a single sulcal region even if it has no primary sulcal branch. However, this quantity is not critical in a resulting shape of the primary sulcal curve since the trajectories from the endpoints of the minor branch curves are significantly overlapped with the primary sulcal curve by the Dijkstra's algorithm (see Fig. 8). The only difference could be the number of minor sulcal branch curves that need to be pruned. This concept is also valid for the maximum angle ϕ of the separation during the endpoint detection.

3) Curve Smoothness and Pruning—The smoothness of the sulcal curves can be controlled by γ . For $\gamma = 1$, the sulcal curves are delineated by following the pure geodesic trajectories. For $\gamma > 1$, the delineated sulcal curves have smooth trajectories along the principal directions. Although there exists no standard smoothness, we found $\gamma = \exp$ generates reasonable smoothness in most cases (see the orbital sulcus in Fig. 6 for example). For the curve pruning, ψ needs to be chosen depending on the application as pointed out in [33]. In our experiment, we set the threshold 5.0 *mm*, 10.0 *mm*, and 15 *mm*. Similar to [33],

we observed that the primary sulcal curves are captured appropriately even in these different threshold settings, while the minor branch curves are detected in 5.0 *mm* as shown in Fig. 8. It is noteworthy that such a pruning process produces a consistent result of the sulcal curve extraction regardless of the number of detected endpoints. In the experiment, we used a relatively conservative threshold of 5.0 *mm* to capture the primary sulcal curves as well as their minor branch curves.

C. Reproducibility

Since no ground-truth sulcal curve was available, we instead measured reproducibility using the average and Hausdorff distance errors for each sulcal curve. Specifically, we measured the average distance error at each sulcal point between two corresponding surfaces (scan and re-scan sessions) and then computed the mean and maximum (Hausdorff) across the average distance errors along each sulcal curve as proposed in [30], [35]. Since the average distance error is asymmetric (one-way) between the corresponding surfaces, we measured the respective distance errors for the corresponding surfaces rather than taking the average of the two measurements. In a similar way, we also measured the Hausdorff distance error of the extracted sulcal curves between two corresponding surfaces. Since these metrics are defined in the Euclidean space, we applied an optimal rigid alignment [53] to two corresponding surfaces to reduce additional measurement errors being introduced by surface misalignment. For comparisons with an existing method, we used [35] with default parameter settings in the remainder of this paper. Fig. 9 and Table II summarize a statistics on these error measurements across all 21 subjects for FreeSurfer and MaCRUISE pipelines, respectively. We observed high reproducibility on average for both the average and Hausdorff distance errors in terms of the original MRI resolution (1.0 *mm*) and the overall higher reproducibility than [35] (approximately 20% relative improvement in error). Also, the statistical *t*-tests revealed significant difference between those two methods in both distance errors for each surface reconstruction model. In addition, TRACE was able to produce comparable results for the two different cortical surface reconstruction pipelines.

D. Robustness to Noise

To evaluate robustness to noise, synthetic noisy (bumpy) surfaces were generated by adding vertex-wise perturbation of existing surface models. We picked the first scan session from each subject in the Kirby reproducibility dataset. Then, perturbations (random displacements) of the vertices were added to the original surfaces. In particular, a displacement at each location follows an independent and identically distributed uniform distribution at maximum of 1.0 *mm* (see Fig. 4 and Fig. 11). This allows each vertex to have a random displacement toward the neighboring voxels in the volume space. However, since the triangle size is much smaller than the noise level, a huge displacement potentially makes a self-intersection of the surfaces, in which a contoured slice could not be well-defined. To prevent the surfaces from being degenerative, we thus resampled the displacements not to allow the vertices to intrude into other triangles. It is noteworthy that such an assumption of the statistical independence could still yield a worse distortion than a practical image acquisition since the distortion is independent of local neighborhoods. Despite the significant noise influences, we observed no noticeable difference from the original surface in most sulcal regions. We used the same error metrics employed for the reproducibility. A

quantitative statistics is summarized in Fig. 10 and Table III. For both pipelines, we achieved higher robustness to noise than [35] at a noise level of 1.0 *mm* (approximately 30% relative improvement in error). Also, the statistical *t*-tests revealed significant difference between those two methods in both distance errors for each surface reconstruction model. Fig. 11 shows example sulcal curves on the noisy surface.

E. Comparison with Manual Delineation

We compared our extracted sulcal curves with the manually delineated primary sulcal curves of the MSC dataset. It is noteworthy that the labeling protocol is completely independent of our method. Since the extracted sulcal curves had no label information, we chose the closest curves for each manually delineated curve and measured the average and Hausdorff distance errors for the evaluation. Fig. 12 summarizes the average, percentile, and Hausdorff distance errors. Overall, the average and Hausdorff distance errors were 1.32 ± 0.35 *mm* and 3.77 ± 1.31 *mm* in TRACE while 1.38 ± 0.46 *mm* and 4.20 ± 1.25 *mm* were observed in [35], respectively. We conducted paired *t*-tests on both errors and found no significant difference between those two methods in the average distance error ($p = 0.0713$) whereas significant difference was revealed in the Hausdorff distance error ($p < 0.0001$). The large distance error was observed typically for two reasons. First, several primary sulcal curves were traced over the gyral regions such as the precentral sulcus (preCS), which is incompatible with our definition of the sulcal curves as shown in Fig. 13. Second, manually delineated curves in the dataset were typically jagged being away from the sulcal fundic regions (see Fig. 13). It is noteworthy that the TRACE algorithm is purely based on the cortical surface geometry. The sulcal points are thus selected based only on a contoured slice associated with principal directions. Since the extracted sulcal curves are obtained along the nearest neighboring sulcal points, it could be also different from the manual delineation although there is no ground-truth or commonly agreed protocol of the sulcal curve delineation.

V. Conclusion

We demonstrated the automatic sulcal curve extraction in two main steps. To select sulcal points, the line simplification method was employed due to its denoising effects that naturally handles surface noise. Sulcal curves were extracted from the candidate sulcal points by applying the Dijkstra shortest path algorithm on a connected graph of the sulcal points with a smoothness constraint. Unlike surface registration-based methods, the TRACE algorithm requires neither any template model nor priori knowledge but rather based on the subject shape-specific geometric information. We discussed different parameter settings and their influences on the resulting curves.

In the experiments, TRACE achieved higher reproducibility and robustness to noise on the Kirby reproducibility dataset than the existing curve extraction method [35]. Also, we observed a comparable reproducibility for the two different surface reconstruction pipelines. For robustness to noise, we added random displacements for each vertex to simulate noise influences on the surfaces. The resulting sulcal curves were extracted consistently compared to those of the corresponding original surfaces in qualitative and quantitative evaluations. Quantitatively, small curve extraction errors were observed for all the subjects in the Kirby

dataset. Moreover, TRACE showed comparable extraction results to the manual delineation of primary sulci in the MSC dataset.

The TRACE algorithm is scalable and versatile. In the main components – sulcal point selection and sulcal curve extraction, their computation at every vertex is independent of each other, which is efficiently improved in parallel processing. The parallel version of TRACE is publicly available². The TRACE algorithm is not limited to sulcal curve extraction. This can be extended to gyral curve extraction as also proposed in [33]. In general, the TRACE algorithm can be applied to any type of surface models (not limited to cortical surfaces) to delineate curves along their ridge/valley regions.

Acknowledgment

The authors would like to thank the Biomedical Imaging Research Lab and Brain and Creativity Institute for providing the MSC dataset and Drs. Li and Liu for sharing their curve extraction tool.

This work was supported by NSF CAREER 1452485, NIH R01EB017230 (Landman), R01MH102266 (Woodward), VICTR/WISE VR3029, the National Center for Research Resources, UL1 RR024975-01, the National Center for Advancing Translational Sciences, UL1 TR000445-06, and NIH MH901645, HD003110, and HD079124 (Styner).

References

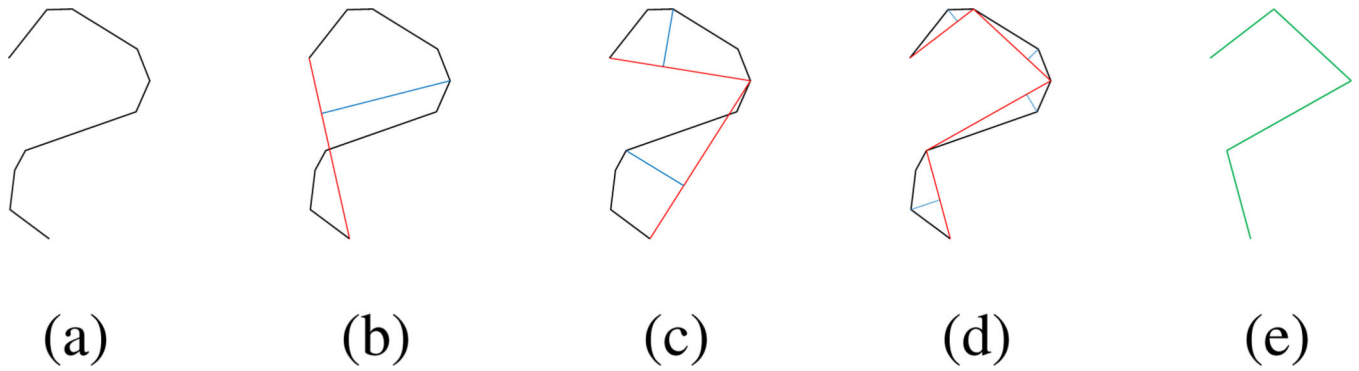
- [1]. Dale AM, Fischl B, and Sereno MI, “Cortical surface-based analysis: I. segmentation and surface reconstruction,” *Neuroimage*, vol. 9, no. 2, pp. 179–194, 1999. [PubMed: 9931268]
- [2]. Kim J, Singh V, Lee J, Lerch J, Ad-Dab’bagh Y, MacDonald D, Lee J, Kim S, and Evans A, “Automated 3-d extraction and evaluation of the inner and outer cortical surfaces using a laplacian map and partial volume effect classification,” *NeuroImage*, vol. 27, no. 1, pp. 210–221, 2005. [PubMed: 15896981]
- [3]. Cointepas Y, Mangin J-F, Garnero L, Poline J-B, and Benali H, “Brainvisa: software platform for visualization and analysis of multimodality brain data,” *Neuroimage*, vol. 13, no. 6, p. 98, 2001.
- [4]. Huo Y, Plassard AJ, Carass A, Resnick SM, Pham DL, Prince JL, and Landman BA, “Consistent cortical reconstruction and multi-atlas brain segmentation,” *NeuroImage*, vol. 138, pp. 197–210, 2016. [PubMed: 27184203]
- [5]. Ono M, Kubik S, and Abernathy CD, *Atlas of the cerebral sulci*. Tps, 1990.
- [6]. Le Goualher G, Procyk E, Collins DL, Venugopal R, Barillot C, and Evans AC, “Automated extraction and variability analysis of sulcal neuroanatomy,” *IEEE transactions on medical imaging*, vol. 18, no. 3, pp. 206–217, 1999. [PubMed: 10363699]
- [7]. Mangin J, Riviere D, Cachia A, Duchesnay E, Cointepas Y, Papadopoulos-Orfanos D, Scifo P, Ochiai T, Brunelle F, and Régis J, “A framework to study the cortical folding patterns,” *NeuroImage*, vol. 23, pp. S129–S138, 2004. [PubMed: 15501082]
- [8]. Thompson PM, Hayashi KM, Sowell ER, Gogtay N, Giedd JN, Rapoport JL, De Zubicaray GI, Janke AL, Rose SE, Semple J et al., “Mapping cortical change in alzheimer’s disease, brain development, and schizophrenia,” *Neuroimage*, vol. 23, pp. S2–S18, 2004. [PubMed: 15501091]
- [9]. Fillard P, Arsigny V, Pennec X, Hayashi KM, Thompson PM, and Ayache N, “Measuring brain variability by extrapolating sparse tensor fields measured on sulcal lines,” *Neuroimage*, vol. 34, no. 2, pp. 639–650, 2007. [PubMed: 17113311]
- [10]. Cachia A, Paillère-Martinot M-L, Galinowski A, Januel D, de Beaupaire R, Bellivier F, Artiges E, Andoh J, Bartrés-Faz D, Duchesnay E et al., “Cortical folding abnormalities in schizophrenia patients with resistant auditory hallucinations,” *Neuroimage*, vol. 39, no. 3, pp. 927–935, 2008. [PubMed: 17988891]

²<https://github.com/ilwoolyu/CurveExtraction>

- [11]. Lyu I, Seong J, Shin S, Im K, Roh J, Kim M, Kim G, Kim J, Evans A, Na D, and Lee J, "Spectral-based automatic labeling and refining of human cortical sulcal curves using expert-provided examples," *NeuroImage*, vol. 52, no. 1, pp. 142–157, 2010. [PubMed: 20363334]
- [12]. De Winter F-L, Zhu Q, Van den Stock J, Nelissen K, Peeters R, de Gelder B, Vanduffel W, and Vandenbulcke M, "Lateralization for dynamic facial expressions in human superior temporal sulcus," *NeuroImage*, vol. 106, pp. 340–352, 2015. [PubMed: 25463458]
- [13]. Leroy F, Cai Q, Bogart SL, Dubois J, Coulon O, Monzalvo K, Fischer C, Glasel H, Van der Haegen L, Bénézit A et al., "New human-specific brain landmark: the depth asymmetry of superior temporal sulcus," *Proceedings of the National Academy of Sciences*, vol. 112, no. 4, pp. 1208–1213, 2015.
- [14]. Lyu I, Kim SH, Bullins J, Gilmore JH, and Styner MA, "Novel local shape-adaptive gyrification index with application to brain development," in *International Conference on Medical Image Computing and Computer-Assisted Intervention*. Springer, 2017, pp. 31–39.
- [15]. Gu X, Wang Y, Chan TF, Thompson PM, and Yau S-T, "Genus zero surface conformal mapping and its application to brain surface mapping," *IEEE Transactions on Medical Imaging*, vol. 23, no. 8, pp. 949–958, 2004. [PubMed: 15338729]
- [16]. Van Essen DC, "A population-average, landmark-and surface-based (pals) atlas of human cerebral cortex," *Neuroimage*, vol. 28, no. 3, pp. 635–662, 2005. [PubMed: 16172003]
- [17]. Joshi AA, Shattuck DW, Thompson PM, and Leahy RM, "Surface-constrained volumetric brain registration using harmonic mappings," *Medical Imaging, IEEE Transactions on*, vol. 26, no. 12, pp. 1657–1669, 2007.
- [18]. Du J, Younes L, and Qiu A, "Whole brain diffeomorphic metric mapping via integration of sulcal and gyral curves, cortical surfaces, and images," *NeuroImage*, vol. 56, no. 1, pp. 162–173, 2011. [PubMed: 21281722]
- [19]. Park H, Park J, Seong J, Na D, and Lee J, "Cortical surface registration using spherical thin-plate spline with sulcal lines and mean curvature as features," *Journal of Neuroscience Methods*, vol. 206, no. 1, pp. 46–53, 2012. [PubMed: 22366330]
- [20]. Auzias G, Lefevre J, Le Troter A, Fischer C, Perrot M, Régis J, and Coulon O, "Model-driven harmonic parameterization of the cortical surface: Hip-hop," *IEEE transactions on medical imaging*, vol. 32, no. 5, pp. 873–887, 2013. [PubMed: 23358957]
- [21]. Datar M, Lyu I, Kim S, Cates J, Styner MA, and Whitaker R, "Geodesic distances to landmarks for dense correspondence on ensembles of complex shapes," in *International Conference on Medical Image Computing and Computer-Assisted Intervention*. Springer, 2013, pp. 19–26.
- [22]. Lyu I, Kim S, Seong J, Yoo S, Evans A, Shi Y, Sanchez M, Niethammer M, and Styner M, "Robust estimation of group-wise cortical correspondence with an application to macaque and human neuroimaging studies," *Frontiers in Neuroscience*, vol. 9, p. 210, 2015. [PubMed: 26113807]
- [23]. Fischl B, van der Kouwe A, Destrieux C, Halgren E, Ségonne F, Salat DH, Busa E, Seidman LJ, Goldstein J, Kennedy D et al., "Automatically parcellating the human cerebral cortex," *Cerebral cortex*, vol. 14, no. 1, pp. 11–22, 2004. [PubMed: 14654453]
- [24]. Desikan RS, Ségonne F, Fischl B, Quinn BT, Dickerson BC, Blacker D, Buckner RL, Dale AM, Maguire RP, Hyman BT et al., "An automated labeling system for subdividing the human cerebral cortex on mri scans into gyral based regions of interest," *Neuroimage*, vol. 31, no. 3, pp. 968–980, 2006. [PubMed: 16530430]
- [25]. Destrieux C, Fischl B, Dale A, and Halgren E, "Automatic parcellation of human cortical gyri and sulci using standard anatomical nomenclature," *Neuroimage*, vol. 53, no. 1, pp. 1–15, 2010. [PubMed: 20547229]
- [26]. Khaneja N, Miller MI, and Grenander U, "Dynamic programming generation of curves on brain surfaces," *IEEE Transactions on Pattern Analysis and Machine Intelligence*, vol. 20, no. 11, pp. 1260–1265, 1998.
- [27]. Kent J, Mardia K, and West J, "Ridge curves and shape analysis," in *The British Machine Vision Conference 1996*, 1996, pp. 43–52.

- [28]. Monga O, Benayoun S, and Faugeras O, "From partial derivatives of 3-d density images to ridge lines," in *Computer Vision and Pattern Recognition, 1992. Proceedings CVPR'92.*, 1992 IEEE Computer Society Conference on. IEEE, 1992, pp. 354–359.
- [29]. Ohtake Y, Belyaev A, and Seidel H-P, "Ridge-valley lines on meshes via implicit surface fitting," *ACM transactions on graphics (TOG)*, vol. 23, no. 3, pp. 609–612, 2004.
- [30]. Le Troter A, Auzias G, and Coulon O, "Automatic sulcal line extraction on cortical surfaces using geodesic path density maps," *NeuroImage*, vol. 61, no. 4, pp. 941–949, 2012. [PubMed: 22521478]
- [31]. Shattuck DW, Joshi AA, Pantazis D, Kan E, Dutton RA, Sowell ER, Thompson PM, Toga AW, and Leahy RM, "Semi-automated method for delineation of landmarks on models of the cerebral cortex," *Journal of neuroscience methods*, vol. 178, no. 2, pp. 385–392, 2009. [PubMed: 19162074]
- [32]. Kao C-Y, Hofer M, Sapiro G, Stern J, Rehm K, and Rottenberg DA, "A geometric method for automatic extraction of sulcal fundi," *Medical Imaging, IEEE Transactions on*, vol. 26, no. 4, pp. 530–540, 2007.
- [33]. Shi Y, Thompson PM, Dinov I, and Toga AW, "Hamilton-jacobi skeleton on cortical surfaces," *Medical Imaging, IEEE Transactions on*, vol. 27, no. 5, pp. 664–673, 2008.
- [34]. Seong J, Im K, Yoo S, Seo S, Na D, and Lee J, "Automatic extraction of sulcal lines on cortical surfaces based on anisotropic geodesic distance," *NeuroImage*, vol. 49, no. 1, pp. 293–302, 2010. [PubMed: 19683580]
- [35]. Li G, Guo L, Nie J, and Liu T, "An automated pipeline for cortical sulcal fundi extraction," *Medical image analysis*, vol. 14, no. 3, pp. 343–359, 2010. [PubMed: 20219410]
- [36]. Ramer U, "An iterative procedure for the polygonal approximation of plane curves," *Computer graphics and image processing*, vol. 1, no. 3, pp. 244–256, 1972.
- [37]. Douglas D and Peucker T, "Algorithms for the reduction of the number of points required to represent a digitized line or its caricature," *Cartographica: The International Journal for Geographic Information and Geovisualization*, vol. 10, no. 2, pp. 112–122, 1973.
- [38]. Dijkstra EW, "A note on two problems in connexion with graphs," *Numer. Math*, vol. 1, no. 1, pp. 269–271, 12 1959 [Online]. Available: 10.1007/BF01386390
- [39]. Lyu I, Kim S, and Styner M, "Automatic sulcal curve extraction on the human cortical surface," in *Medical Imaging 2015: Image Processing*, vol. 9413 SPIE, 2015, pp. 941 324–1–941 324–7.
- [40]. Reggiori GB, "Digital computer transformations for irregular line drawings," DTIC Document, Tech. Rep, 1972.
- [41]. Hershberger J and Snoeyink J, "Speeding up the douglas-peucker line-simplification algorithm," in *In 5th Intl. Symp. on Spatial Data Handling, 1992*, pp. 134–143.
- [42]. Tsitsiklis JN, "Efficient algorithms for globally optimal trajectories," *IEEE Transactions on Automatic Control*, vol. 40, no. 9, pp. 1528–1538, 1995.
- [43]. Sethian JA, "A fast marching level set method for monotonically advancing fronts," *Proceedings of the National Academy of Sciences*, vol. 93, no. 4, pp. 1591–1595, 1996.
- [44]. Sethian JA and Vladimirsky A, "Ordered upwind methods for static hamilton-jacobi equations: Theory and algorithms," *SIAM Journal on Numerical Analysis*, vol. 41, no. 1, pp. 325–363, 2003.
- [45]. Koenderink JJ, *Solid Shape*. Cambridge, MA, USA: MIT Press, 1990.
- [46]. Meyer M, Desbrun M, Schröder P, and Barr AH, "Discrete differential-geometry operators for triangulated 2-manifolds," in *Visualization and mathematics III*. Springer, 2003, pp. 35–57.
- [47]. Damon J, "Swept regions and surfaces: modeling and volumetric properties," *Theoretical Computer Science*, vol. 392, no. 1, pp. 66–91, 2008.
- [48]. Landman BA, Huang AJ, Gifford A, Vikram DS, Lim IAL, Farrell JA, Bogovic JA, Hua J, Chen M, Jarso S et al., "Multi-parametric neuroimaging reproducibility: a 3-t resource study," *Neuroimage*, vol. 54, no. 4, pp. 2854–2866, 2011. [PubMed: 21094686]
- [49]. Joshi AA, Pantazis D, Li Q, Damasio H, Shattuck DW, Toga AW, and Leahy RM, "Sulcal set optimization for cortical surface registration," *Neuroimage*, vol. 50, no. 3, pp. 950–959, 2010. [PubMed: 20056160]

- [50]. Pantazis D, Joshi A, Jiang J, Shattuck DW, Bernstein LE, Damasio H, and Leahy RM, "Comparison of landmark-based and automatic methods for cortical surface registration," *Neuroimage*, vol. 49, no. 3, pp. 2479–2493, 2010. [PubMed: 19796696]
- [51]. Rettmann ME, Han X, Xu C, and Prince JL, "Automated sulcal segmentation using watersheds on the cortical surface," *NeuroImage*, vol. 15, no. 2, pp. 329–344, 2002. [PubMed: 11798269]
- [52]. Lebed E, Jacova C, Wang L, and Beg MF, "Novel surface-smoothing based local gyrification index," *Medical Imaging, IEEE Transactions on*, vol. 32, no. 4, pp. 660–669, 2013.
- [53]. Besl PJ, McKay ND et al., "A method for registration of 3-d shapes," *IEEE Transactions on pattern analysis and machine intelligence*, vol. 14, no. 2, pp. 239–256, 1992.

**Fig. 1.**

A schematic overview of the line simplification method. (a)-(b) Given a planar curve, a horizontal line (*red*) is obtained by finding the two farthest points, from which the extremal point is selected having the farthest distance (*blue*). (c)-(d) The extremal point is then employed to define a new horizontal line and the procedure is recursively applied until below a tolerance. (e) The final simplified line is obtained by connecting all the detected extremal points.

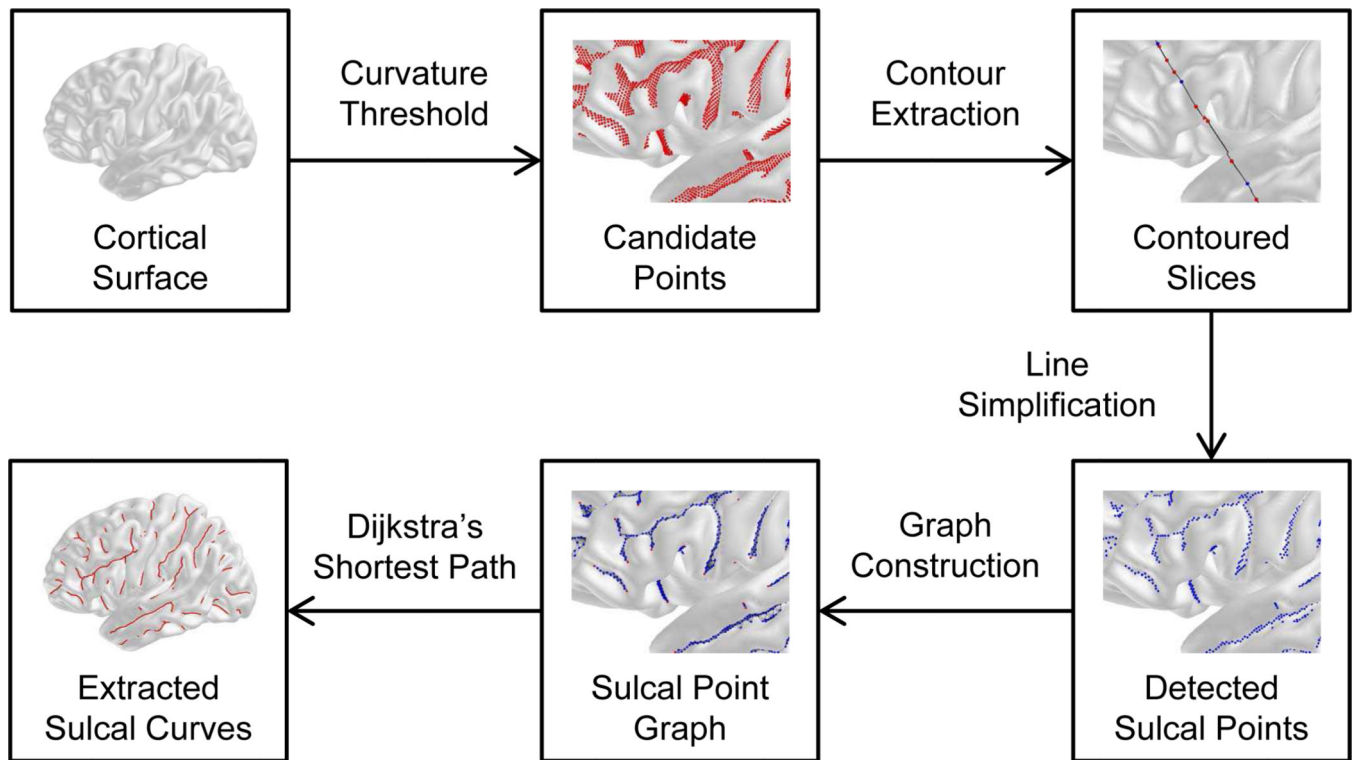


Fig. 2.

A schematic overview of the TRACE algorithm. A set of candidate points is selected by thresholding the principal curvature map on the cortical surface. The line simplification method determines stable sulcal points from the detected candidate points. The sulcal points are connected to create a partially connected graph. The Dijkstra's shortest path algorithm is then applied on the graph to obtain a complete set of the sulcal curves.

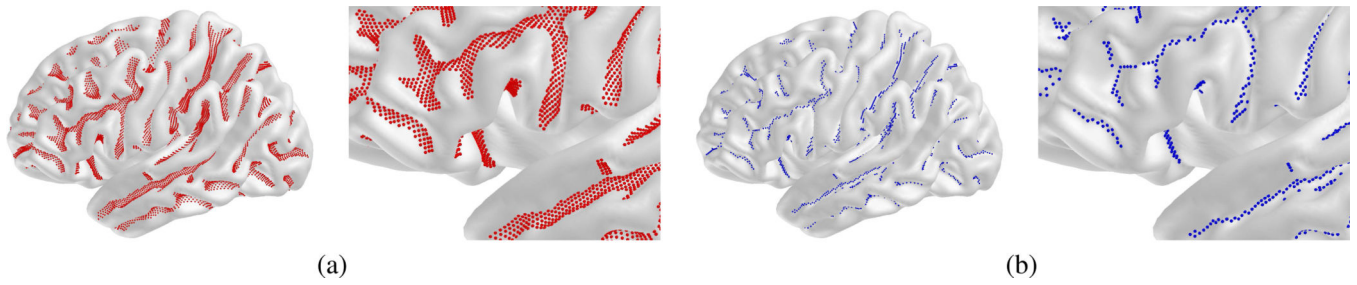


Fig. 3. Sulcal point detection: (a) positive maximum curvature points and (b) selected sulcal points. The vertices with positive maximum curvatures are selected for candidate sulcal points. Since the candidate vertices are spread over a large portion of the sulcal fundic regions, they are further filtered out by the line simplification method that eventually selects sulcal points (*blue*).

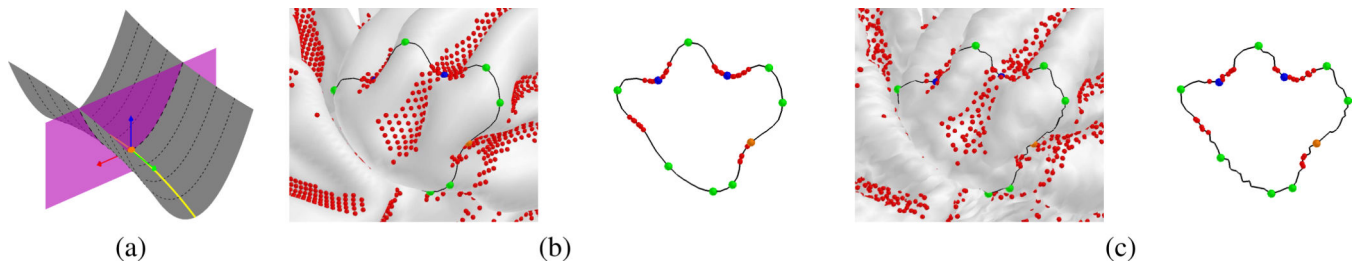


Fig. 4.

Contour extraction at a given candidate point and extremal points of the contour. (a) A schematic illustration of the contour extraction indicates several cutting planes (*dot lines*) with respect to the first and second principal directions (*red* and *green*). (b) The contour represents the maximal surface bending at a candidate point (*orange*). The line simplification method selects a minimum sufficient number of the extremal points – the convex (*green*) and concave (*blue*) points that are part of the original contour. (c) The line simplification method selects sulcal points in the presence of noise in a robust way even if several candidate points (*red*) exist around sulcal points. The candidate point becomes a sulcal point if it is selected as an extremal point after the line simplification.

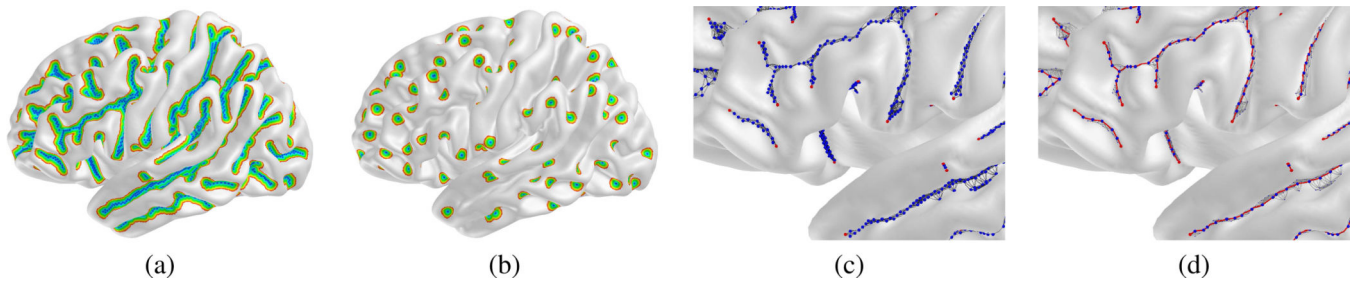


Fig. 5.

Graph construction and endpoints: (a) the geodesic radial regions ($r = 4.0 \text{ mm}$), (b) the geodesic radial regions of the endpoints ($r = 4.0 \text{ mm}$), (c) a partial graph G of the sulcal points, and (d) shortest paths (*red* curves) on G . A partial graph of the sulcal points is constructed within the geodesic radial regions. The endpoints of G are determined if their neighboring sulcal points are skewed within the geodesic radial regions. The shortest paths are computed between endpoints on G .

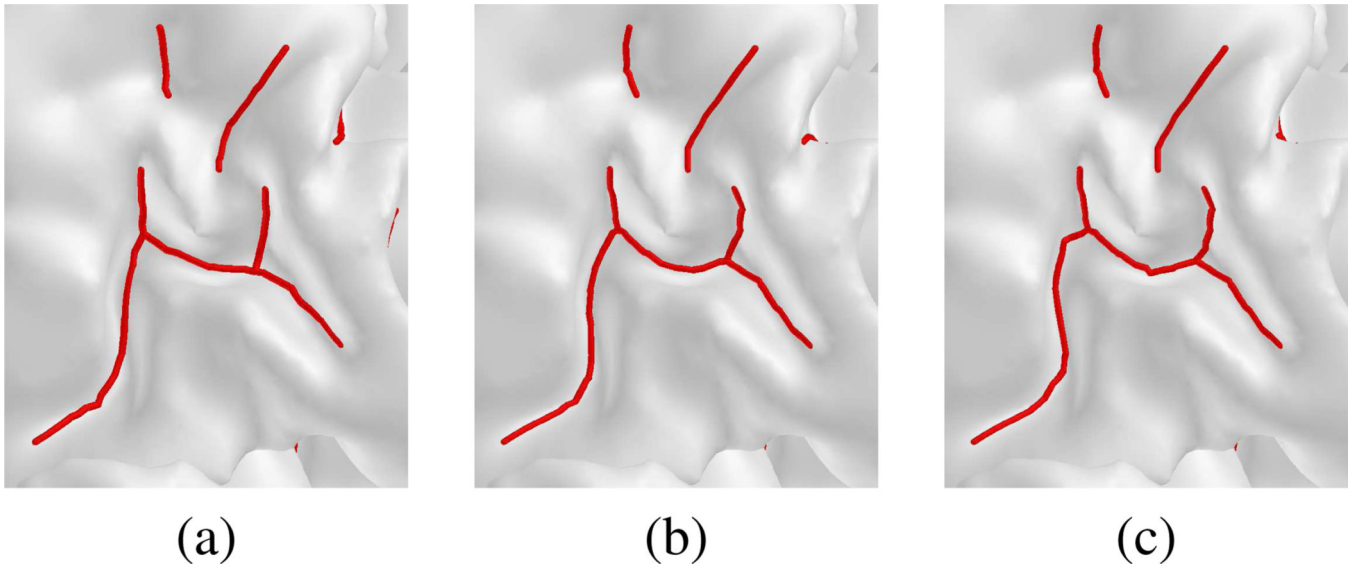


Fig. 6. Curve smoothness varying at (a) $\gamma = 1$, (b) $\gamma = e$, and (c) $\gamma = e^4$. The edge weights encode only geodesic distances for $\gamma = 1$. The geodesic path is relatively stiff compared to the curvature weighted trajectories $\gamma > 1$ (b)-(c). For large γ , the extraction of the sulcal curves becomes sensitive to the local tangent estimation.

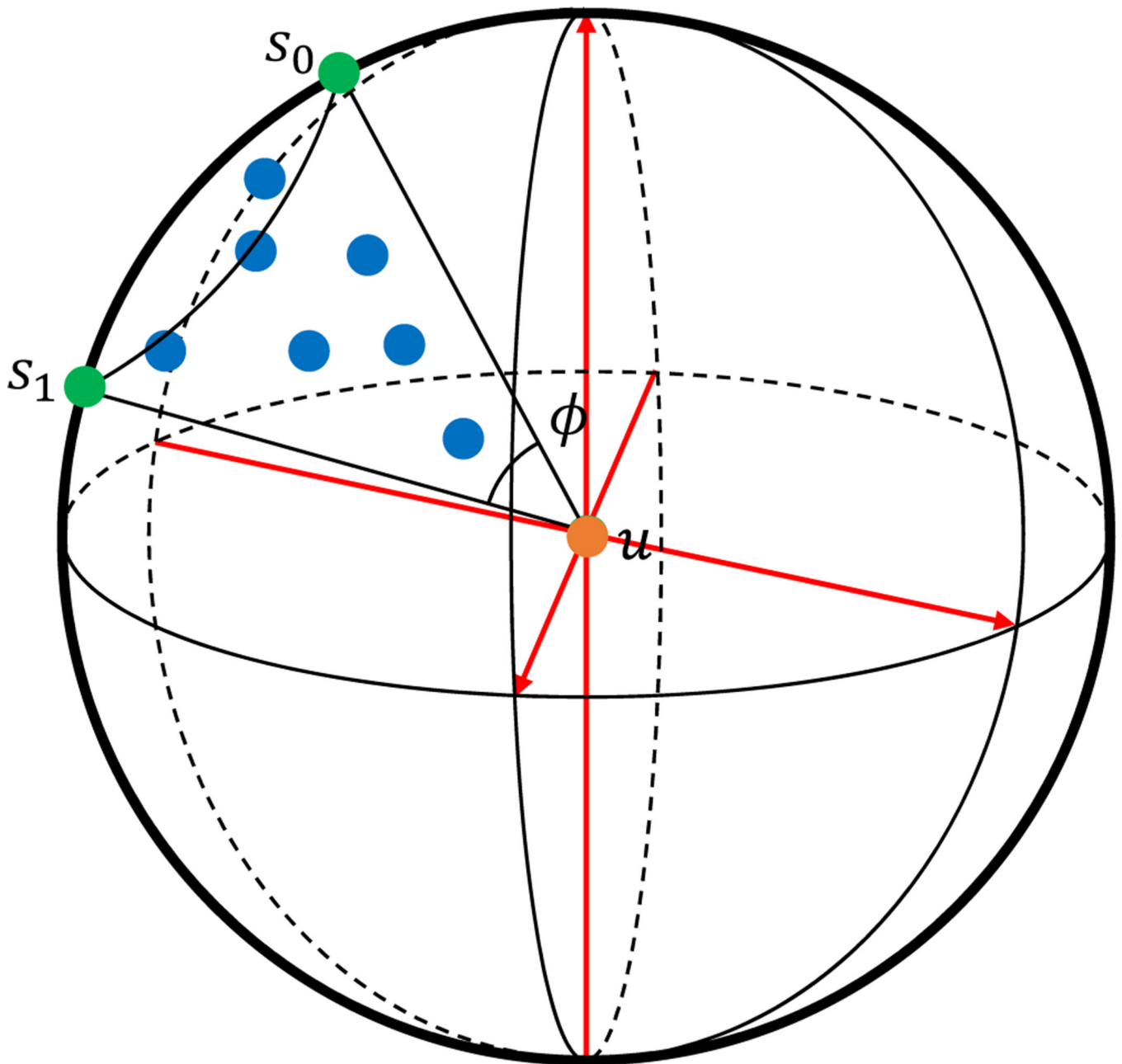


Fig. 7. A schematic illustration of the proposed endpoint detection. \mathbf{u} is determined as an endpoint if its neighboring sulcal points within a geodesic kernel $R_r(\mathbf{u})$ belong to a spherical cone. Two vectors $(\mathbf{s}_0 - \mathbf{u})$ and $(\mathbf{s}_1 - \mathbf{u})$ form the maximum angle ϕ across every possible line starting from \mathbf{u} .

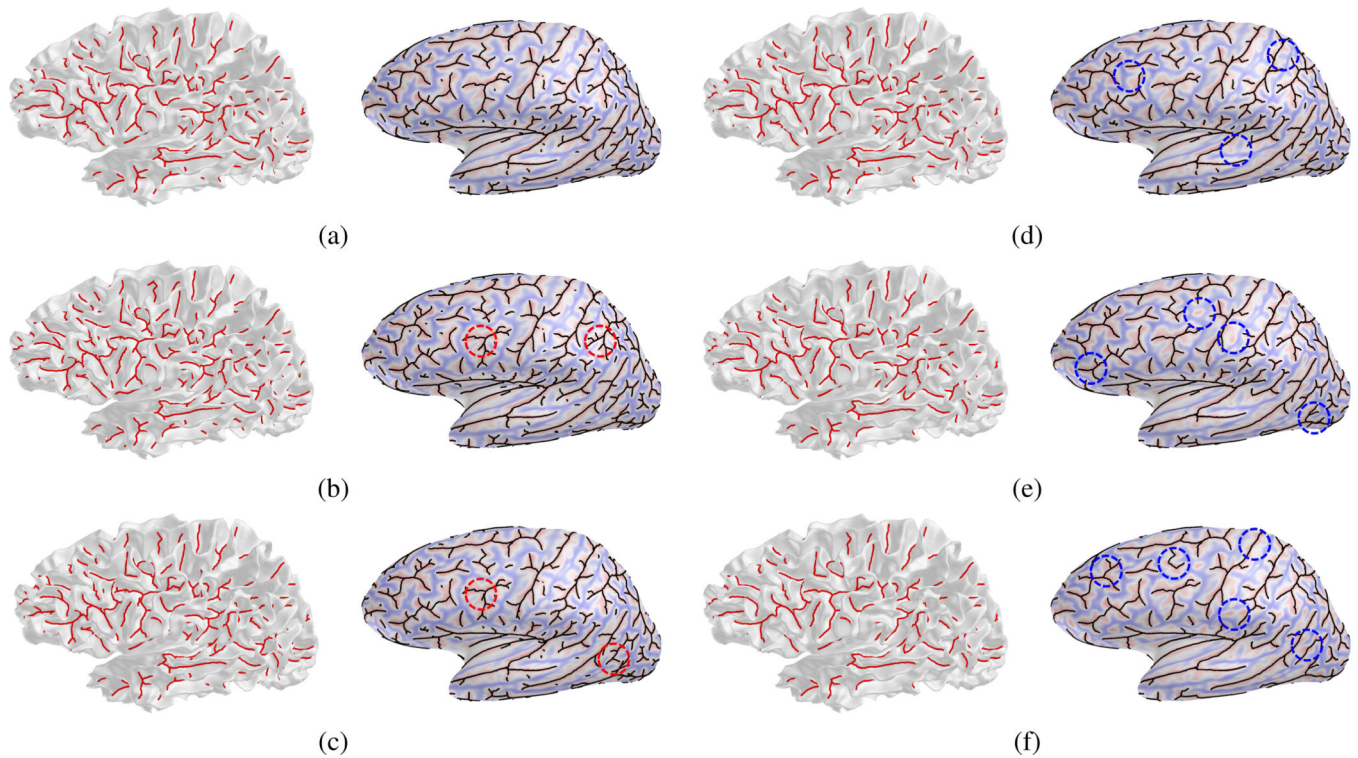


Fig. 8. Different settings of the curve parameters: (a) $\delta = 2.5 \text{ mm}$, $r = 4.0 \text{ mm}$ (suggested setting without pruning), (b) $\delta = 1.5 \text{ mm}$, $r = 4.0 \text{ mm}$, (c) $\delta = 2.5 \text{ mm}$, $r = 2.0 \text{ mm}$, (d) $\psi = 5.0 \text{ mm}$, (e) $\psi = 10.0 \text{ mm}$, and (f) $\psi = 15.0 \text{ mm}$. (b) The primary curves are delineated along the sulcal regions while the curve length is little extended and additional minor branch curves are extracted for $\delta = 1.5 \text{ mm}$. (c) A similar behavior is observed to the line simplification threshold. For both parameter settings, the primary sulcal curves are well preserved. (d)-(f) The minor sulcal branch curves are pruned with an increasing threshold. The primary sulcal curves remain the same across all the thresholds, whereas most minor branch curves are retained in 5.0 mm . The *red* and *blue* circles indicate minor branch and pruned curves, respectively. The white matter/inflated surfaces are used for better visualization.

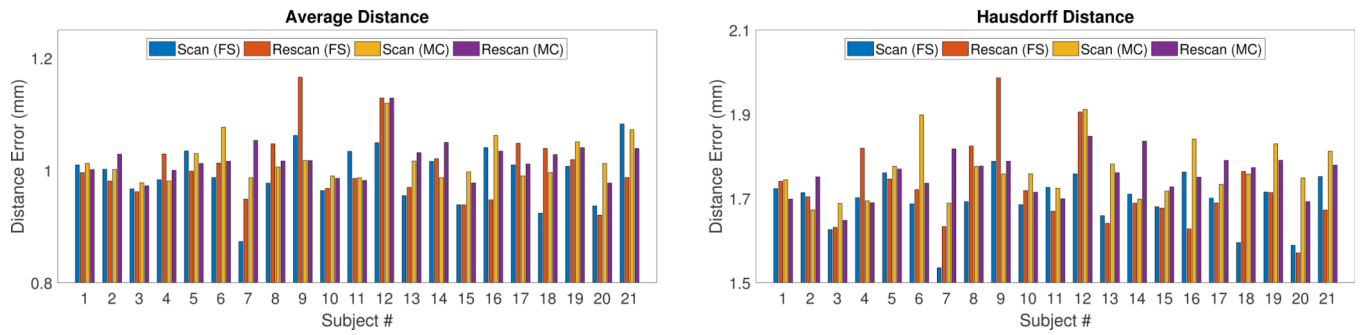


Fig. 9. Reproducibility on the Kirby reproducibility dataset for FreeSurfer (FS) and MaCRUISE (MC). Overall, high reproducibility is achieved for all the subjects. Even for the Hausdorff distance error metric, TRACE shows quite stable reproducibility. The maximum average and Hausdorff distances are less than 1.2 mm and 2.0 mm , respectively, given an MRI resolution (1.0 mm).

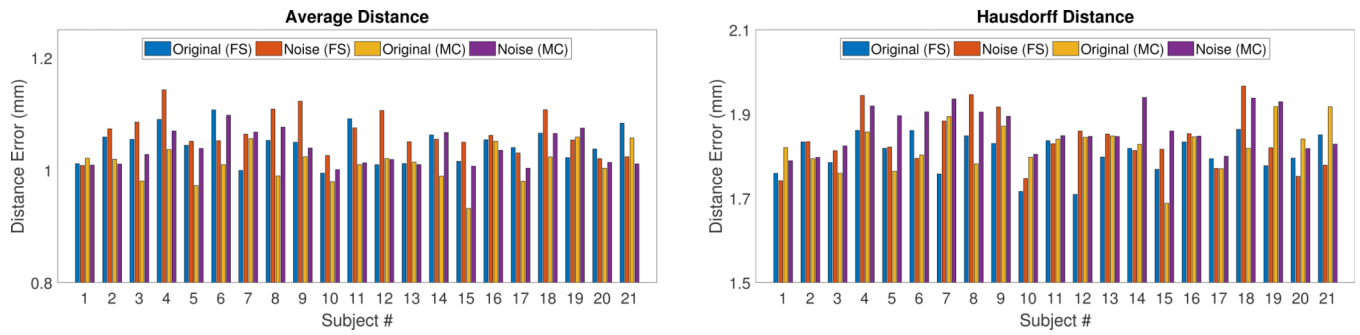


Fig. 10.

Robustness to noise at a noise level of 1.0 mm for FreeSurfer (FS) and MaCRUISE (MC). Even in the presence of significant artificial noise, the TRACE algorithm quite consistently extracts sulcal curves with small curve extraction errors. The maximum average and Hausdorff distances are less than 1.2 mm and 2.0 mm , respectively, given a noise level (1.0 mm).

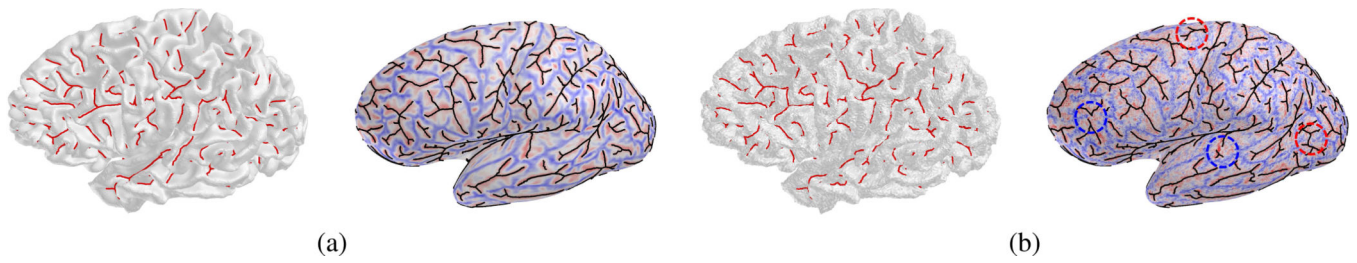


Fig. 11. Robustness to noise at the noise level of 1.0 *mm*: (a) original surface and (b) noisy surface. The mean curvature maps on the inflated surfaces show smoothness of the surfaces. Due to the significant noise influences, several minor sulcal branch curves are introduced (*red*) or not detectable (*blue*) on the noisy surface. However, they are still quite consistently extracted qualitatively and quantitatively.

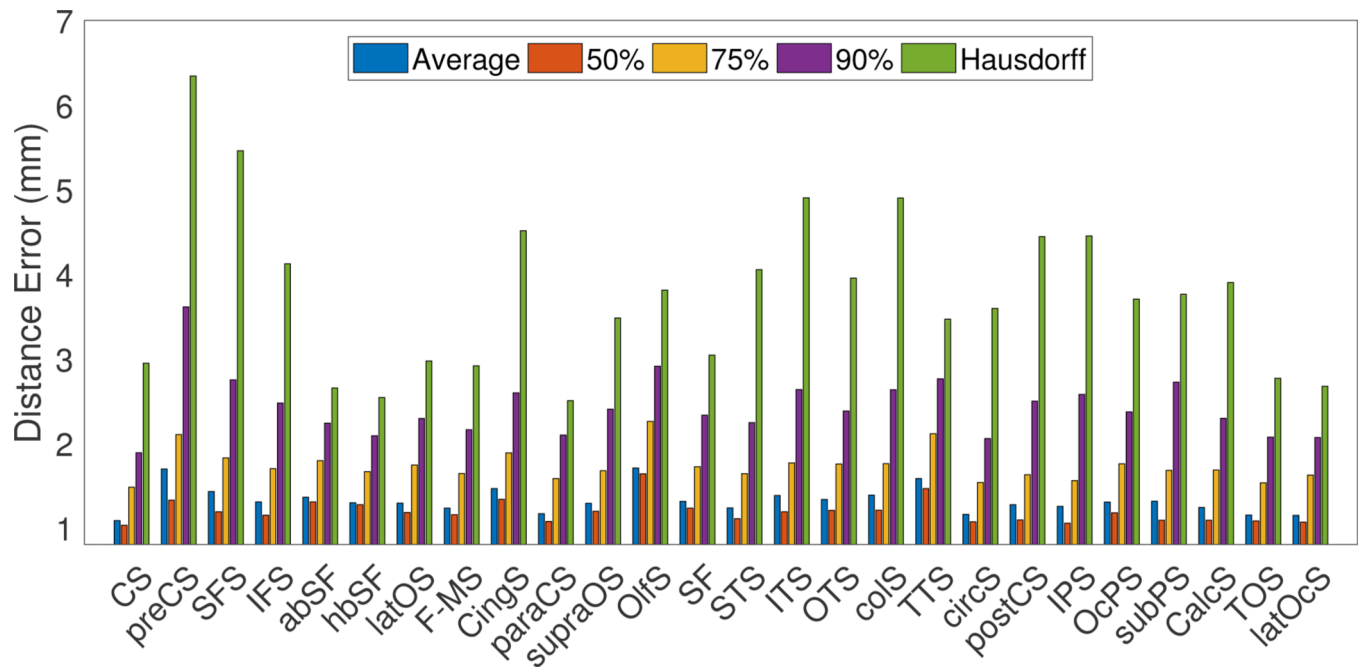


Fig. 12.

Distance errors between the manual delineation and the extracted curves by TRACE on 26 primary sulcal curves. The average distance error is 1.32 *mm* for all the primary sulci. Large distance errors are observed mainly because the manual delineation is jagged and traced over the gyral regions.

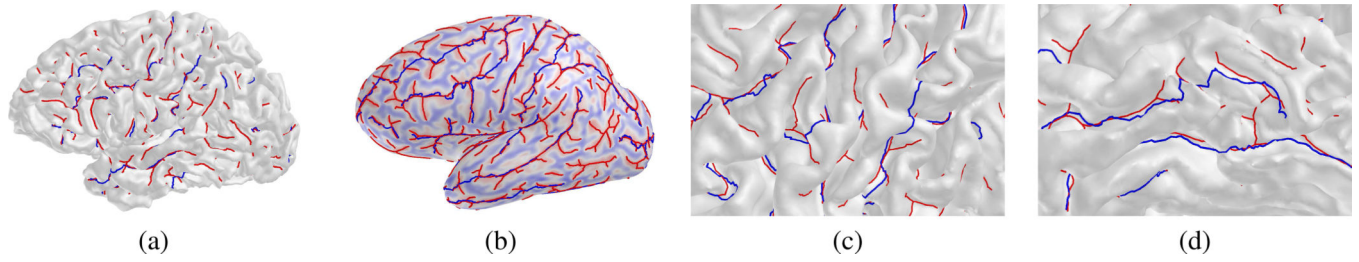


Fig. 13.

TRACE (*red*) and manual delineation (*blue*): (a) sulcal curves on the original surface, (b) sulcal curves on the inflated surface, (c) the motor cortex, and (d) the temporal lobe. The manual delineation is jagged and traced over the gyral regions, which increases distance errors.

TABLE I

Glossary of Parameters

| parameter | description |
|-----------|---|
| δ | smallest deviation for line simplification |
| r | kernel size of geodesic functional for graph construction |
| φ | maximum angle for endpoint detection |
| γ | smoothness of sulcal curves |
| ψ | threshold for minor curve pruning |

Author Manuscript

Author Manuscript

Author Manuscript

Author Manuscript

TABLE II

Reproducibility on 21 subjects in Kirby dataset

| surface model | method | average distance | | | | Hausdorff distance | | | |
|----------------|-----------------------|------------------|-------|------|------|--------------------|-------|------|------|
| | | mean | stdev | min | max | mean | stdev | min | max |
| FreeSurfer [1] | TRACE | 1.00* | 0.89 | 0.87 | 1.17 | 1.71* | 1.15 | 1.54 | 1.99 |
| | Li <i>et al.</i> [35] | 1.23 | 0.91 | 0.87 | 3.28 | 1.94 | 1.13 | 1.54 | 4.23 |
| MaCRUISE [4] | TRACE | 1.02** | 0.89 | 0.97 | 1.13 | 1.76** | 1.18 | 1.65 | 1.91 |
| | Li <i>et al.</i> [35] | 1.29 | 1.39 | 1.14 | 1.45 | 2.63 | 1.73 | 2.39 | 2.83 |

(UNIT: mm, * $p < 0.005$, ** $p < 0.0001$)

Author Manuscript

Author Manuscript

Author Manuscript

Author Manuscript

TABLE III

Robustness to noise on 21 subjects in Kirby dataset

| surface model | method | average distance | | | | Hausdorff distance | | | |
|----------------|-----------------------|------------------|-------|------|------|--------------------|-------|------|------|
| | | mean | stdev | min | max | mean | stdev | min | max |
| FreeSurfer [1] | TRACE | 1.06** | 0.95 | 0.99 | 1.14 | 1.82** | 1.18 | 1.71 | 1.97 |
| | Li <i>et al.</i> [35] | 1.42 | 1.41 | 1.21 | 1.62 | 2.72 | 1.60 | 2.18 | 3.29 |
| MaCRUISE [4] | TRACE | 1.02** | 0.94 | 0.93 | 1.10 | 1.84** | 1.21 | 1.69 | 1.94 |
| | Li <i>et al.</i> [35] | 1.53 | 1.61 | 1.38 | 1.71 | 3.08 | 1.82 | 2.71 | 3.55 |

(UNIT: mm, ** $p < 0.0001$)

Author Manuscript

Author Manuscript

Author Manuscript

Author Manuscript